Ceramics



Effect of nano-TiO₂ on C–S–H phase distribution within Portland cement paste

Ange-Therese Akono^{1,*} (D)

¹ Department of Civil and Environmental Engineering, Department of Mechanical Engineering, Northwestern University, 2145 Sheridan Road, Evanston, IL 60208, USA

Received: 7 April 2020 Accepted: 17 May 2020

© Springer Science+Business Media, LLC, part of Springer Nature 2020

ABSTRACT

We investigate the mechanisms by which titanium dioxide nanoparticles (nano-TiO₂) interact with cement hydration products. To this end, we synthesize nanomodified cement samples with 1 wt% and 5 wt% of TiO2. We investigate the physical properties using depth-sensing-based methods such as statistical nanoindentation and microscopic scratch testing. Fourier transform infrared spectroscopy yields the chemistry, whereas micromechanics modeling provides insights into the nanostructure. The macroscopic plane strain modulus increases by 16% and 83%, respectively, and the macroscopic indentation hardness increases by 37% and 40%, respectively. The fracture toughness rises by 3% and 11%, respectively. Environmental scanning electron microscopy reveals a 30% reduction in crack width for TiO₂ cement nanocomposites compared to plain cement. Meanwhile, Fourier transform infrared spectroscopy and statistical deconvolution show an increase in the fraction of high-density calcium silicate hydrates (by 22% and 12%, respectively), and in the fraction of calcium hydroxide (by 101% and 251%, respectively). Within the framework of the colloidal and granular models of C-S-H, the increase in stiffness and strength after nano-TiO₂ modification of cement paste is due to the closely packed structure and the high atomic coordination number of high-density C-S-H. Similarly, due to the high dimensional stability of high-density C-S-H and calcium hydroxide, our results explain the reported improvements in drying shrinkage and creep properties following cement modification with nano-TiO₂.

Introduction

In recent years, nanoparticles have received a lot of attention as a means to boost the performance of fresh and hardened cement paste. For instance, studies have shown that nanoalumina particles can increase the tensile strength and flexural strength of concrete and reduce the setting time [1]. Nanoscale modification with nanosilica particles has been linked to increased compressive strength [2], increased flexural strength and compressive strength in cement

 $Address\ correspondence\ to\ E-mail:\ Ange-therese. a kono@northwestern.edu$

[3–5], and increased compressive strength in fly-ash cement systems [6, 7].

We focus on titanium dioxide nanoparticles (nano-TiO₂). These nanofillers can increase the photocatalytic and self-cleaning properties of cementitious materials [8–10]. Moreover, nano-TiO₂ can improve the compressive strength of cement [11, 12], increase the flexural strength [13–15], and shorten the setting time [12, 16]. Nano-TiO₂ can also increase the torque and initial yield stress [17], decrease the water absorption and water permeability coefficients [18], and reduce the drying shrinkage [19].

However, the mechanisms by which nanoparticles, in general, and TiO₂ nanoparticles (nano-TiO₂), in particular, enhance the properties of cement are not fully understood. It is agreed that nanoparticles can accelerate cement hydration [13, 15, 16, 19–21], contribute to eliminating large pores [14, 19, 22], and help to refine the pore structure [12, 16, 18, 19]. Yet, the influence of nanoparticles on cement hydration products is subject to debate. Some researchers reported an increase in calcium hydroxide formation at early ages [13, 15, 22], whereas others reported the opposite trend [6, 16, 23]. Thus, advanced studies are needed to understand how nanoparticles modify cement at the nanometer length scale.

Our research objective is to investigate the influence of TiO₂ nanoparticles on the mechanical properties, on the pore structure, and the distribution of hydrated products in Portland cement paste. To this end, we employ nanoscale mechanical characterization methods such as grid nanoindentation and microscopic scratch testing integrated with advanced analytical techniques such as X-ray diffraction and Fourier transform infrared spectroscopy. First, we present our synthesis procedure, and then, we detail our experimental protocols and the underlying theoretical frameworks; finally, we describe our results and discuss their significance.

Materials and methods

Materials

We synthesized cement composites reinforced with titanium dioxide nanoparticles (nano-TiO₂). To this end, Portland cement I was mixed with deionized water containing dispersed TiO₂. Nano-TiO₂ was provided by US Nano (US Research Nanomaterials

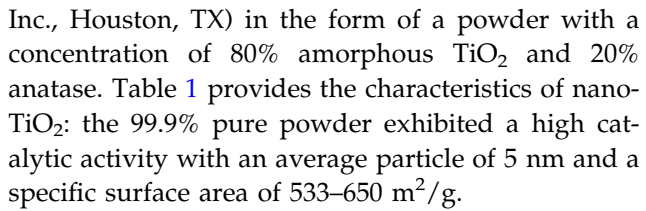


Table 2 provides the mix proportions for the TiO₂modified cement nanocomposites. The water-to-cement ratio was fixed equal to w/c = 0.44. Along with a reference sample, specimen TN0, two weight fractions of TiO2 were considered: 1% wt for specimen TN1, and 5% wt for specimen TN5. We employed ultrasonic energy to disperse the TiO₂ nanoparticles in deionized water with an ultrasonic liquid processor VCX 750; the total provided ultrasonic energy was 2.89 kJ per gram of nano-TiO2. Afterward, the mixture of nano-TiO2 dispersed in deionized water was mixed with Portland cement I using an IKA overhead stirrer for 2 min. The mixing speed was 300 rpm, for specimens TN0 and TN1. However, for specimen TN5, the mixing speed was 800 rpm to overcome the increase in viscosity.

Afterward, the resulting slurry was cast into lubricated 30 mm cylindrical plastic molds, tapped to release macroscopic air bubbles, covered with polyethylene films, and left to cure on an orbital shaker set at 100 rpm for 24 h at 22 ± 2 °C. After 24 h of initial curing, the specimens were removed from their molds and stored in sealed containers full of deionized water for an additional 6 days at 22 ± 2 °C. At the end of the curing stage, the 7-day-old cement nanocomposites were soaked in ethanol for 24 h to stop cement hydration, wrapped in polyethylene films, and stored in plastic containers inside hermetically sealed cabinets to prevent drying and shrinkage.

Table 1 Characteristics of titanium dioxide nanoparticles (nano-TiO₂) used to modify cement specimens

Purity, %	99.9
Average particle size, nm	5
Specific surface area, m ² /g	533-650
Bulk density, g/cm ³	0.12-0.18
True density, g/cm ³	3.9



Table 2 Mix proportions for TiO₂-modified cement nanocomposites

Sample	TN0	TN1	TN5
Cement, g	69.44	69.44	69.44
Deionized water, g	30.56	30.56	30.56
Nano-TiO ₂ , g	0	0.69	3.47
Nano-TiO ₂ , %wt	0	1	5

Grinding and polishing

We utilized a thorough grinding and polishing procedure that yielded high-quality surfaces with low surface roughness, which is an essential requirement to perform high-accuracy nanoscale mechanical testing. First, we embedded the cement nanocomposites in low-viscosity epoxy resin under vacuum. Second, 5-mm-thick slices were machined using a low-speed diamond saw and later mounted onto 30 mm aluminum disks using cyanoacrylate adhesive. We ground the specimens using a semiautomated grinder polisher in concert with silicon carbide grinding pads with particle size 50 µm, 18.3 µm, 10.6 µm, and 7.8 µm. For polishing, we used silicon carbide abrasive lapping discs with particle size, 3 μm, 1 μm, and 0.25 µm. In between each step, we cleansed the specimens in N-decane using an ultrasonic bath and dried them using compressed air. At the end of the grinding and polishing procedure, we stored the polished samples in vacuum desiccators until further testing.

Analytical methods: SEM and FTIR

We conducted Fourier transform infrared analysis to study the chemistry of the TiO_2 -modified cement nanocomposites. First, powder specimens were generated by grinding bulk cement specimens with a McCrone mill with ethanol and sieved down to a particle size < 44 μ m. Infrared spectra were collected using the KBr technique (which consists of mixing 0.1 mg of powder sample with 10 mg of KBr); we used a Nicolet iS50 Nicolet iS50 spectrometer (Thermo Nicolet) spectrometer in regular adsorption–transmission mode with a frequency range from 4000 to 400 cm $^{-1}$ and a resolution of 4 cm $^{-1}$.

Environmental scanning electron microscopy imaging was conducted on uncoated specimens using an FEI Quanta 650 environmental electron

scanning microscope under low vacuum. The accelerating voltage was set at 15 kV, using a walking distance of 12 mm and a spot size of 5.3.

Microscopic scratch testing

We used microscopic scratch tests to probe the fracture response, as shown in Fig. 1. To this end, we employed an Anton Paar microscopic scratch tester equipped with a Rockwell C diamond probe with a 200 µm tip radius. During each test, the vertical force increased linearly, thanks to a feedback loop, from 0.03 N up to 2 N over a scratch length of 3 mm at a loading rate of 3.94 N/min. Before testing, a surface profilometer assessed the surface with a prescan load of 0.03 N. During the test, high-accuracy force transducers recorded the horizontal and vertical forces with a resolution of 0.1 mN. Meanwhile, displacement transducers measured the penetration depth with a resolution of 0.3 nm. At the end of each test, a high-resolution Nikon optical microscope captured a panorama view of the top residual surface. For each specimen, we conducted N = 12 individual scratch tests. All testing took place in an

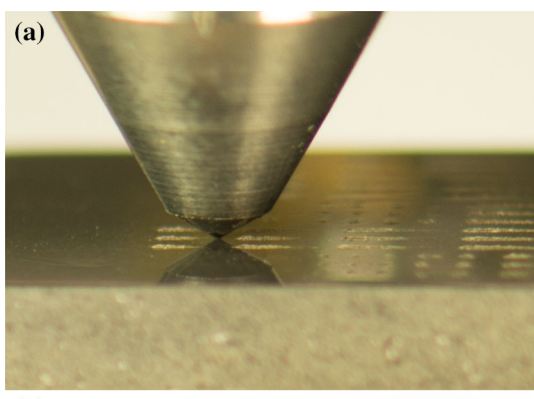




Figure 1 a Digital photography image of a scratch test on a heterogeneous material. Credit: Ange-Therese Akono, Northwestern University, 2019. **b** Schematic representation of a scratch test.



environmental chamber at a temperature of 22 ± 2 °C.

We applied nonlinear fracture mechanics to compute the fracture toughness from the force and penetration depth measurements. The theoretical model was derived using the *J*-integral: an observer tied to the tip of the moving crack computes the energy release rate from their perspective. Using analytical solutions of the stress and strain field functions provided by the Airy stress function method, the final expression relating the fracture toughness to the horizontal force and the penetration depth reads [24, 25]:

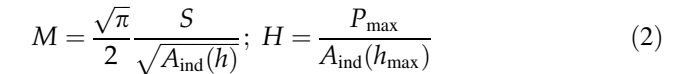
$$\frac{F_T}{\sqrt{2pA(d)}} \le K_c \tag{1}$$

where 2pA is the scratch probe shape, which is dependent on both the scratch probe geometry and the penetration depth. For a spherical probe of tip radius R, 2pA is a quadratic function of the penetration depth: $2pA/R^3 = \alpha \left(\frac{d}{R}\right)^2$. The coefficient α is calibrated using a material of reference such as fused silica.

Grid nanoindentation

We conducted grid nanoindentation tests using an Anton Paar NHT² nanohardness tester to capture the spatial distribution of the mechanical properties. For each polished specimen—TN0, TN1, and TN5—a 15×15 indentation grid was conducted with an inter-indent spacing of 20 μm , thereby spanning an area of 280 $\mu m \times 280~\mu m$.

For each indentation test, the prescribed maximum vertical load was 2 mN, the loading/unloading rate was 4 mN/min, and the holding phase lasted 10 s. A patented passive surface referencing system was used to detect the surface. During each test, force sensors and displacement sensors recorded the vertical load P and the penetration depth d with a resolution of 20 nN for the load and 0.01 nm for the displacement, and at an acquisition rate of 40.0 kHz. For all indentation tests, the indenter was a Berkovich probe of tip radius 2 nm. All tests were conducted inside an environmental chamber at a controlled temperature of 22 \pm 2 °C. For each indentation test, the indentation modulus M and the indentation hardness H were computed by application of the Oliver & Pharr method [26, 27]:



where S is the initial slope of the load–depth curve upon unloading, and A_{ind} is the indenter contact surface area function, which is calibrated prior to testing using fused silica as a reference material.

An important question is to correlate the local values of the indentation modulus M and indentation hardness H to the underlying structure. Assuming that each indentation probes a local volume that behaves as a porous composite, we apply nonlinear micromechanics solutions that connect the indentation modulus M and indentation hardness H to the local packing density η and to the intrinsic mechanical characteristics of calcium–silicate hydrates: skeleton indentation modulus m_s , skeleton Poisson's ratio v_s , skeleton internal friction coefficient α_s , and skeleton cohesion c_s . Thus, we have:

$$M = m_{\rm s} \mathcal{M}(\nu_{\rm s}, \eta, \eta_0) \tag{3}$$

$$H = c_{\rm s} \kappa(\eta, \eta_0, \alpha_{\rm s}) \tag{4}$$

where η_0 is the percolation threshold that depends on the morphology. For instance, for a statistically disordered morphology, $\eta_0 = 0.5$. \mathcal{M} is the indentation modulus linear upscaling function that also depends on the morphology. For example, assuming a statistically disordered morphology with spherical grains, an Eshelby-based self-consistent scheme can be used to compute \mathcal{M} . In particular, for $v_s = 0.2$, we have: $\mathcal{M}(v_s = 0.2, \eta, \eta_0 = 0.5) = 2\eta - 1$ [28]. Similarly, κ is the indentation hardness nonlinear upscaling function. κ is computed via cohesive frictional hardness-packing density upscaling schemes. One way to approach this problem is to integrate variational methods such as the linear comparison composite method with finite element schemes to yield a pointby-point evolution of κ [28, 29].

We performed a cluster analysis to identify different micro-constituents based on their mechanical signature. We work in a 3D design space where the local variable includes the local indentation hardness and modulus along with the local value of the packing density $X_{i,1 \le i \le 225} = (M_i; H_i; \eta_i)$. The statistical deconvolution approach aims to represent the experimental probability distribution function as a weighted sum of individual chemo–mechanical phases. We assume a Gaussian distribution of the mechanical properties where each phase j is



characterized by seven parameters: volume fraction fj, average value μ_j^X , and standard deviation s_j^X of variable $X=(M;H;\eta)$. For indents on hydrated cement phases, we expect to measure at least four chemo–mechanical phases: micropores or capillary pores, low-density calcium silicate hydrates, high-density calcium–silicate hydrates, and calcium hydroxide. Therefore, we set n=5. We then implemented a nonlinear constrained minimization algorithm to solve for the $7\times n$ unknowns $\left\{f_j,\mu_j^Ms_j^M,\mu_j^H,s_j^H,\mu_j^\eta,s_j^\eta\right\}$ according to [28, 30]:

$$\min \sum_{i=1}^{N=225} \sum_{X=(M,H,\eta)} \left(\sum_{j=1}^{n=5} f_j F(X_i, \mu_j^X, s_j^X) - F_X(X_i) \right)^2.$$
(5)

We implemented three constraints. The first constraint states that all volume fraction values should add up to unity: $\sum_{j=1}^{n=5} f_j = 1$. The second constraint enforces a sufficient gap to prevent any significant overlap between neighboring individual Gaussian distributions: $\mu_j^X + s_j^X \le \mu_{j+1}^X - s_{j+1}^X, X = (M; H; \eta)$. Finally, the third constraint reduces the risk of spurious phases: $f_i \le 0.05$.

Upscaling of elasto-plastic properties

We employed nonlinear micromechanics to compute the macroscopic plane strain modulus of cement nanocomposites. Given the indentation grid size, 15×15 , with an inter-indent spacing of $20 \mu m$, we consider the volume probed as a composite made of N = 225 phases. For each phase, the indentation modulus M_i is measured locally during nanoindentation testing. Using a self-consistent scheme, the macroscopic plane strain modulus M^{hom} is then given by [29]:

$$\sum_{i=1}^{N=225} \frac{1}{1 + \frac{1}{2} \left(\frac{M_i}{M^{\text{hom}}} - 1 \right)} = \sum_{i=1}^{N=225} \frac{\frac{M_i}{M^{\text{hom}}}}{1 + \frac{1}{2} \left(\frac{M_i}{M^{\text{hom}}} - 1 \right)}.$$
 (6)

We solved Eq. (6) recursively using a numerical scheme. Meanwhile, we approximated the macroscopic indentation hardness H^{hom} by the Voigt–Reuss upper bound:

$$H^{hom} \le \frac{1}{N} \sum_{i=1}^{N=225} H_i.$$

Results

Macroscopic elasto-plastic properties

Nano-TiO₂ significantly enhances the macroscopic elasto-plastic properties, macroscopic plane strain modulus M^{hom} , and macroscopic indentation hardness H^{hom} . Figure 2 displays the evolution of M^{hom} and H^{hom} as a function of the weight fraction of nano-TiO₂. The computed macroscopic plane strain modulus for plain cement w/c = 0.44 is 17.50 GPa. Adding 1 wt% and 5 wt% of nano-TiO₂ leads to, respectively, a 16% and an 83% increase in the macroscopic plane strain modulus. Meanwhile, adding 1 wt% and 5 wt% of nano-TiO₂ leads to,

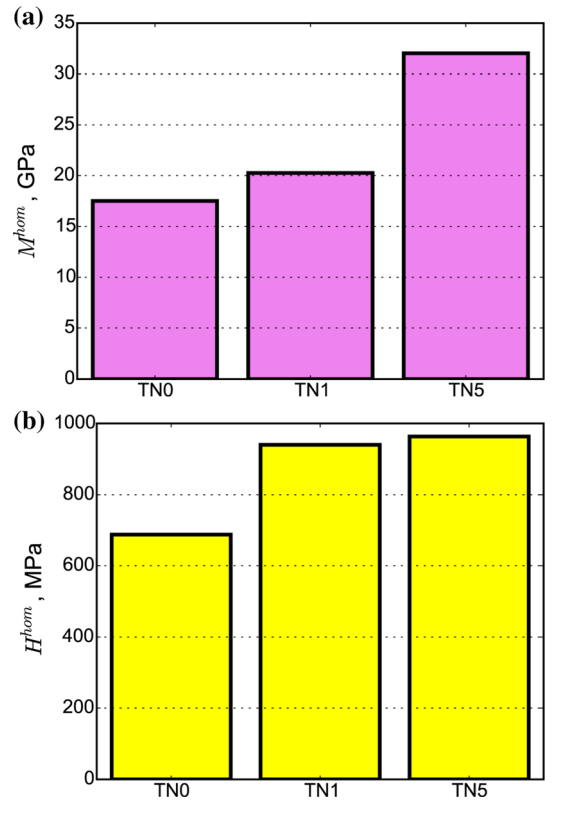


Figure 2 a Macroscopic plane strain modulus M^{hom} as a function of nano-TiO₂ content. **b** Macroscopic indentation hardness H^{hom} as a function of nano-TiO₂ content. TN0 = plain cement. TN1 = cement + 1 wt% TiO₂. TN5 = cement + 5 wt% TiO₂.



respectively, a 37% and a 40% increase in the macroscopic indentation hardness.

Fracture response

Figure 3 displays representative load–depth curves for plain cement (TN0), cement + 1 wt% TiO₂ (TN1), and cement + 5 wt% TiO₂ (TN5). Overall, the horizontal force F_T is a monotonically increasing function of the penetration depth d. The maximum penetration depth is recorded for plain cement at 25.00 μ m, whereas the maximum penetration depth for TN1 and TN5 is, respectively, 24.14 μ m and 22.01 μ m.

The next step is to calculate the fracture toughness from the horizontal force F_T and penetration depth dmeasurements, using Eq. (1). Figure 4a displays the individual scratch test curves for plain cement paste. The quantity $F_T/\sqrt{2pA}$ is displayed as a function of the scratch path *X* for each scratch test conducted on plain cement. All tests superimpose nicely on top of each other, pointing to the repeatability of scratch tests. We observe a convergence of the quantity $F_T/\sqrt{2pA}$ toward a horizontal asymptote for large values of X and hence for large penetration depths. This convergence of $F_T/\sqrt{2pA}$ is due to a regime change from a ductile mode to a brittle regime, where the mechanical energy is dissipated primarily via brittle fracture processes. Figure 4b displays the residual groove after a single scratch test on plain cement. The residual groove, whose width increases due to increases in penetration depth, is evidence of material removal processes. In the brittle regime, the

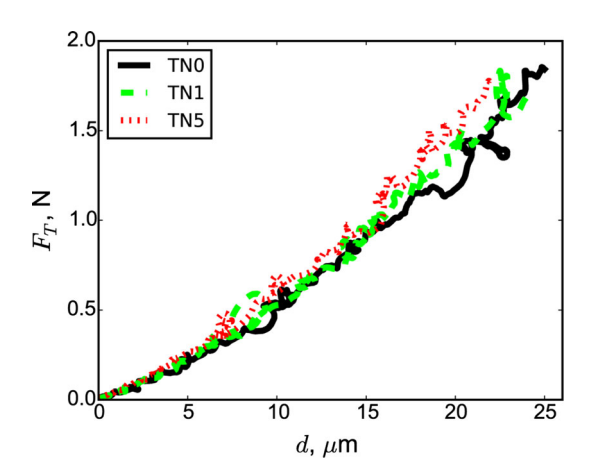


Figure 3 Representative load–depth curves during a scratch test on Portland cement paste reinforced with TiO_2 nanoparticles. F_T is the horizontal force, and d is the penetration depth..



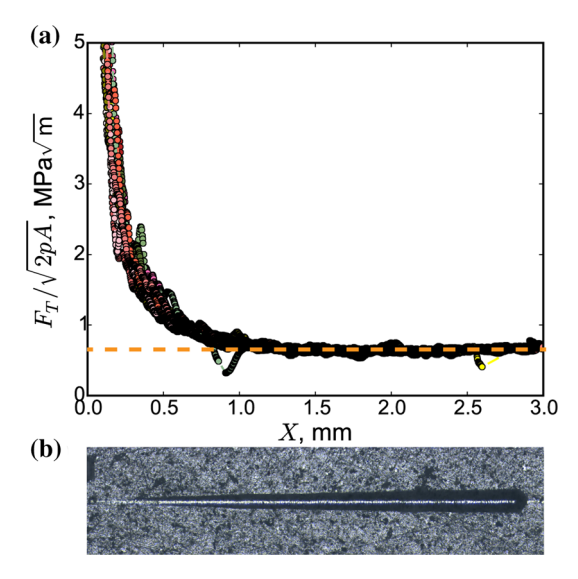


Figure 4 a Scratch test response of plain cement. N = 12 individual scratch tests are represented. F_T is the horizontal force, 2pA is the scratch probe shape function, and X is the scratch path. The dotted horizontal asymptote represents the fracture toughness. **b** Residual groove after a single scratch test on plain cement.

fracture toughness is given by the value of the horizontal asymptote, following Eq. (1).

Thus, using our nonlinear fracture mechanics model, the fracture toughness of plain cement is computed as $K_c(\text{plain cement}) = 0.65 \pm 0.01 \, \text{MPa} \sqrt{\text{m}}$. For plain cement w/c = 0.44, the measured fracture toughness is very close to the literature values [31, 32]. These literature fracture toughness values for cement paste were derived using three-point bending tests jointly with size effect methods. Thus, we have a rigorous and validated approach to characterize the fracture behavior.

Figure 5 investigates the influence of TiO_2 nanoparticles on the fracture toughness of TiO_2 -modified cement paste. The fracture toughness of specimen TN1 is 0.67 ± 0.02 MPa $\sqrt{\text{m}}$, and that of specimen TN5 is 0.72 ± 0.03 MPa $\sqrt{\text{m}}$. The addition of 1 wt% TiO $_2$ nanoparticles yields a 3% increase in the fracture toughness, whereas the addition of 5 wt% TiO $_2$ nanoparticles yields an 11% increase in the fracture toughness. Thus, nano-TiO $_2$ enhances the resistance of cement paste to crack propagation.

Figure 6 compares the fracture micromechanisms of plain Portland cement and that of Portland cement paste modified with 5 wt% nano-TiO₂. To this end, we employed environmental backscattered electron microscopy imaging on uncoated specimens after

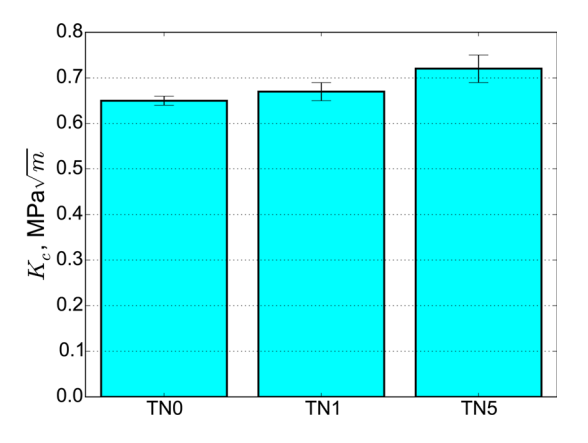


Figure 5 Influence of TiO_2 nanoparticles on fracture toughness K_c values. N = 12 tests were performed per specimen.

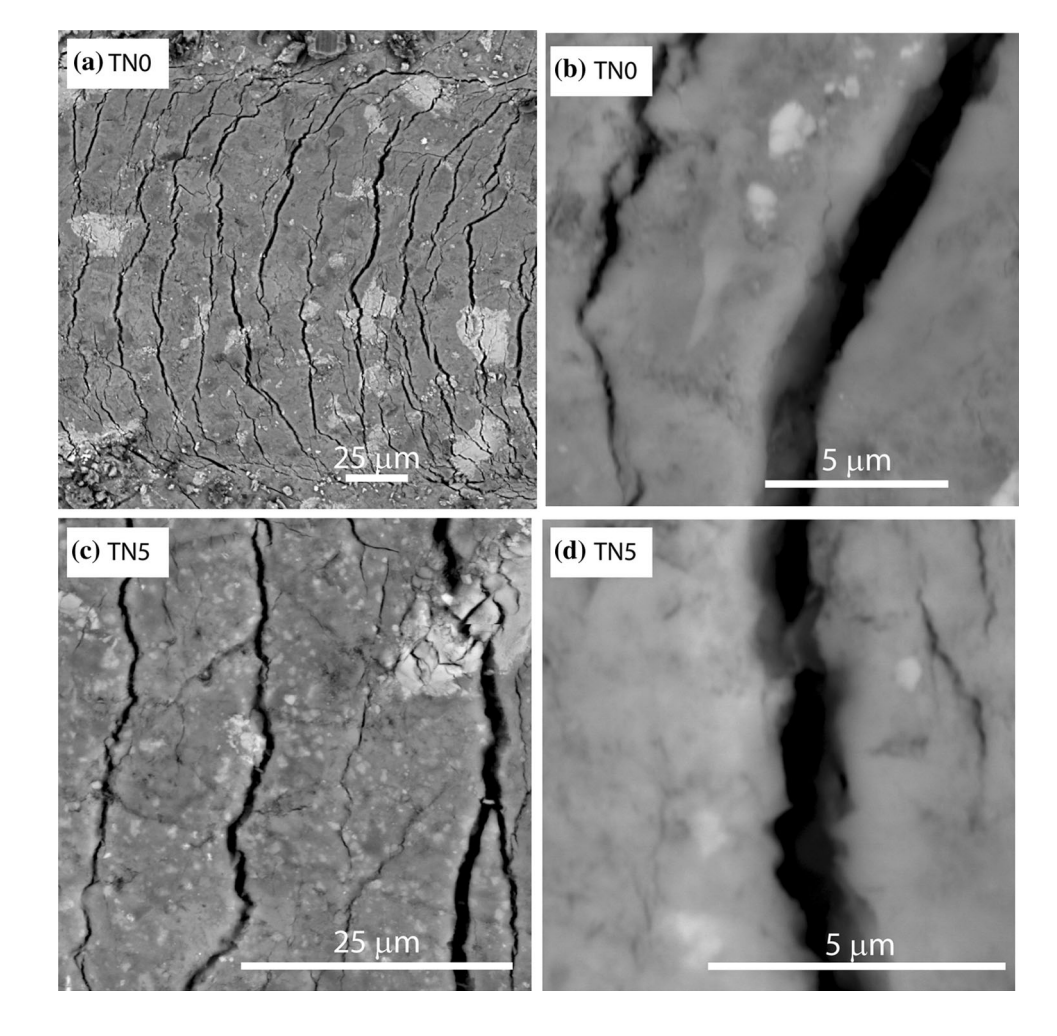
scratch testing, with magnification levels ranging from $709 \times to 16821 \times .$ On plain cement, we observe the formation of semi-circular curved cracks perpendicular to the direction of the scratch probe. Figure 6a displays several fracture micromechanisms for plain cement: micro-cracking, crack deflection, and

Figure 6 Fracture micromechanisms for a, b TN0 specimen and c, d TN5 specimen.

ligament bridging. We also observe the presence of debris on the scratch groove. Figure 6b shows a close-up of a single micro-crack with a crack width of 1.3 μ m. For TN5 (see Fig. 6c), we observe the presence of micro-cracking, crack branching, and ligament bridging. A close-up of a single micro-crack (see Fig. 6d) reveals a crack width of 0.8 μ m. Thus, we observe similar fracture micromechanisms between plain cement and TiO₂-modified cement with a 30% reduction in micro-crack width.

Microstructure

To further understand the influence of nano-TiO₂ on the microstructure of cement nanocomposites, we compute the local packing density using Eqs. (3, 4). We calibrated the intrinsic properties at the skeleton level using plain cement paste; we found: $v_s = 0.2$, $m_s = 63.50\,\text{GPa}$, $c_s = 264.0\,\text{MPa}$, and $\alpha_s = 0.3$. In particular, the computed value of the skeleton indentation modulus m_s agrees with reported values of the





indentation modulus for the calcium silicate hydrate solid using molecular dynamics simulations [33, 34]. Using the calculated mechanical properties for the C–S–H solid, we then calculated the local packing density values for the remaining specimens, TN1 and TN5. The nonlinear upscaling functions $M(\eta)$ and $H(\eta)$ for all three specimens are provided in the Supplementary Materials. Figure 7 displays the histogram of the local packing density η for both plain cement and TiO₂-modified Portland cement nanocomposites.

Nano-TiO₂ induces changes in the distribution of the local packing density. The median value of η is 0.69, 0.69, and 0.75, respectively, for TN0, TN1, and TN5. For plain cement, the histogram of η exhibits two peaks at 0.52, and 0.68. For TN1, the histogram of η exhibits two peaks at 0.56, and 0.72. Finally, for TN5, the peaks of the local packing density are distributed around 0.60 and 0.78. Thus, nano-TiO₂ contributes to an increase in the local packing density and a densification of cement paste.

Chemo-mechanical phases

We employed statistical deconvolution methods to understand further the influence of nano-TiO₂ on the distribution of calcium silicate hydrate products. To this end, we utilize Vandamme and Ulm's multiscale

model for cement paste [28]. At the microscale, cement paste consists of capillary pores, calcium hydroxide (CH), and a nanoporous C-S-H matrix. In turn, the C-S-H matrix is composed of two phases: low-density C-S-H (LD C-S-H) and high-density C-S-H (HD C-S-H). These two C-S-H phases are compositionally similar but structurally distinct. Referring to Jennings' colloidal model for the C-S-H gel [35-37], both low-density C-S-H and high-density C-S-H are composed of globules, \sim 5 nm in size. The C-S-H globules are arranged in a disordered fashion for low-density C-S-H and in a closely packed order for high-density C-S-H. Due to their different packing orders, low-density C-S-H and high-density C-S-H exhibit different values of the packing density, respectively, 0.64 and 0.74 [38]. In turn, these C-S-H phases can be probed based on their unique mechanical signature.

Figure 8 displays the chemo–mechanical phase distribution computed following the statistical deconvolution analysis. As shown, hydrated cement exhibits four phases: micropores or capillary pores, low-density C–S–H, high-density C–S–H, and calcium hydroxide. The optimized packing density values are in the range 0.66–0.67 for low-density C–S–H, 0.71–0.74 for high-density C–S–H, and 0.79–0.83 for calcium hydroxide. For each specimen, Table 3

Figure 7 Packing density distribution in **a** TN0 specimen, **b** TN1 specimen, and **c** TN5.

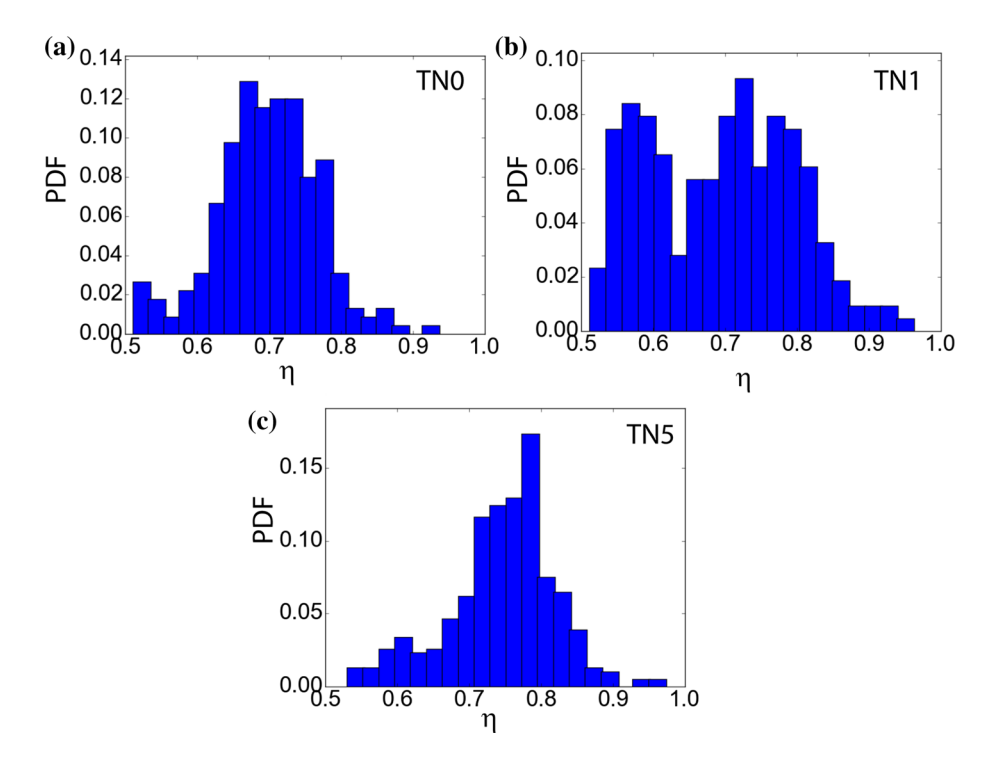
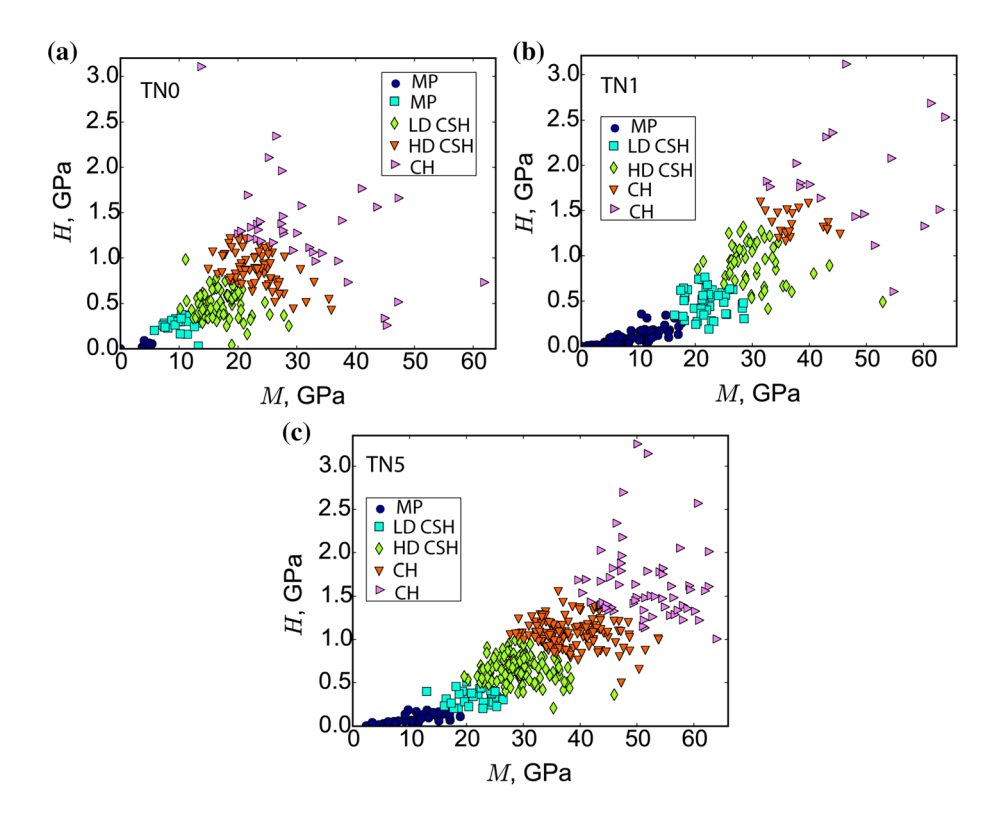




Figure 8 Chemo-mechanical phase distribution of Portland cement TiO₂ nanocomposites. MP = micropores. LD CSH = low-density C–S–H. HD CSH = high-density C–S–H. CH = calcium hydroxide.



lists the indentation modulus and indentation hardness for each chemo-mechanical phase. Furthermore, the Supplementary Materials document provides the graphs of the probability distribution functions of the indentation modulus, of the indentation hardness, and of the local packing density.

The nanoscale modification of cement paste using nano-TiO₂ affects the proportion of hydrated cement

Table 3 Phase distribution computed via a statistical deconvolution analysis of grid nanoindentation data

Phase	$f_j(\%)$	M(GPa)	H(GPa)	η
TN0				
Micropores	5	2.68 ± 2.72	0.00 ± 0.10	0.52 ± 0.03
Micropores	9	9.62 ± 2.73	0.20 ± 0.10	0.60 ± 0.03
LD C-S-H	43	16.52 ± 3.78	0.48 ± 0.18	0.66 ± 0.03
HD C-S-H	31	24.01 ± 3.71	0.89 ± 0.20	0.73 ± 0.03
CH	13	35.60 ± 7.88	1.33 ± 0.21	0.79 ± 0.03
TN1				
Micropores	40	9.07 ± 6.79	0.11 ± 0.21	0.57 ± 0.05
LD C-S-H	16	21.38 ± 4.07	0.51 ± 0.18	0.67 ± 0.03
HD C-S-H	26	29.87 ± 4.42	0.94 ± 0.25	0.74 ± 0.03
CH	11	38.74 ± 4.12	1.40 ± 0.20	0.80 ± 0.03
CH	7	50.46 ± 7.60	2.03 ± 0.36	0.86 ± 0.03
TN5				
Micropores	11	11.93 ± 5.66	0.00 ± 0.16	0.58 ± 0.04
LD C-S-H	7	21.10 ± 3.50	0.29 ± 0.13	0.64 ± 0.03
HD C-S-H	35	29.42 ± 4.82	0.65 ± 0.22	0.71 ± 0.03
CH	33	39.75 ± 5.51	1.07 ± 0.20	0.77 ± 0.03
СН	13	53.18 ± 5.63	1.49 ± 0.22	0.83 ± 0.03

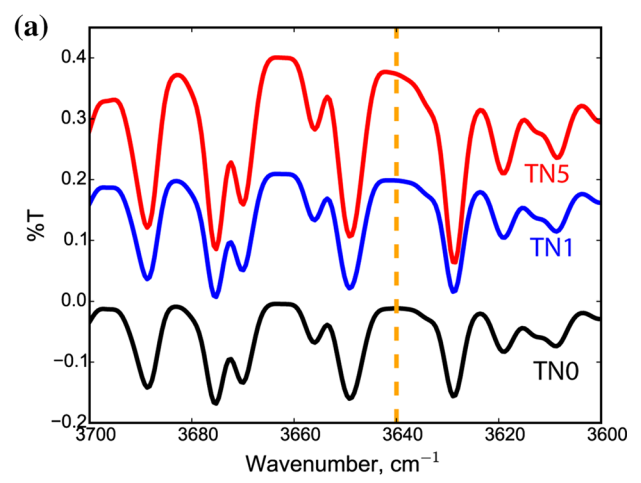
LD C-S-H low density C-S-H, HD C-S-H high density C-S-H, CH calcium hydroxide



phases. Figure 8 shows a qualitative increase in calcium hydroxide and high-density C–S–H. Figure 9 displays the relative fractions of low-density C–S–H, high-density C–S–H, and calcium hydroxide. The relative fraction of calcium hydroxide is tripled from 14.9% for the TN0 specimen to 30.0% for the TN1 specimen and to 52.3% for the TN5 specimen. The fraction of high-density C–S–H increases from 35.6% for TN0 to 43.3% for TN1, and 39.8% for TN5. In turn, the fraction of low-density C–S–H is drastically cut down from 49.4% in TN0 to 26.7% in TN1 and to a mere 8.0% for TN5. Thus, nano-TiO₂ promotes the growth of calcium hydroxide and high-density C–S–H.

FTIR spectra

Figure 10 displays the FTIR spectra for plain cement and TiO₂-modified cement nanocomposites. The addition of nano-TiO2 results in modifications in the FTIR spectra. For both TN1 and TN5, we observe an increase in the intensity of the 3640 cm⁻¹ band. This band is shown in dotted orange in Fig. 10a and is caused by the Ca-OH vibrations in calcium hydroxide. The increase in intensity at the 3640 cm⁻¹ band suggests a higher fraction of calcium hydroxide. Another sharp increase in intensity is observed at the 660-670 cm⁻¹ band. This band is characteristic of Si-O-Si bending vibrations within C-S-H gels, and the observed increase supports the hypothesis of increased C-S-H formation. We have shown the full FTIR spectra in the Supplementary Materials document. Thus, we employed three techniques to study the impact of nano-TiO₂ on cement chemistry: FTIR, nanoindentation, and statistical deconvolution. The three techniques converge in their insights: nano-TiO2 fosters C-S-H and CH formation.



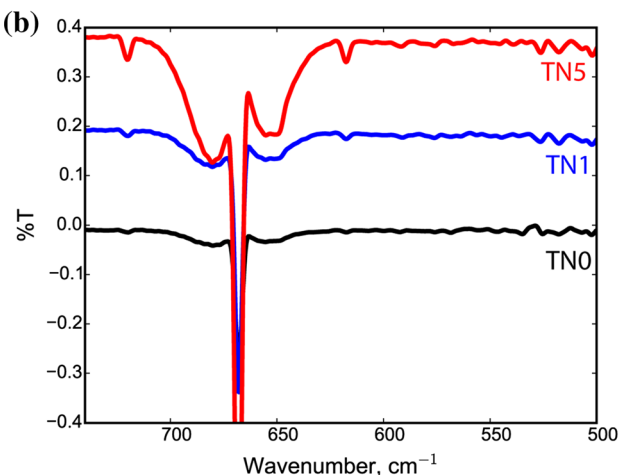


Figure 10 FTIR Spectra for both plain cement (TN0), cement + 1 wt% TiO2 (TN1), and cement + 5 wt% TiO2. **a** The dotted orange line highlights the band at 3640 cm⁻¹ which results from the Ca–OH vibrations in calcium hydroxide. Data courtesy of Jiaxin Chen.

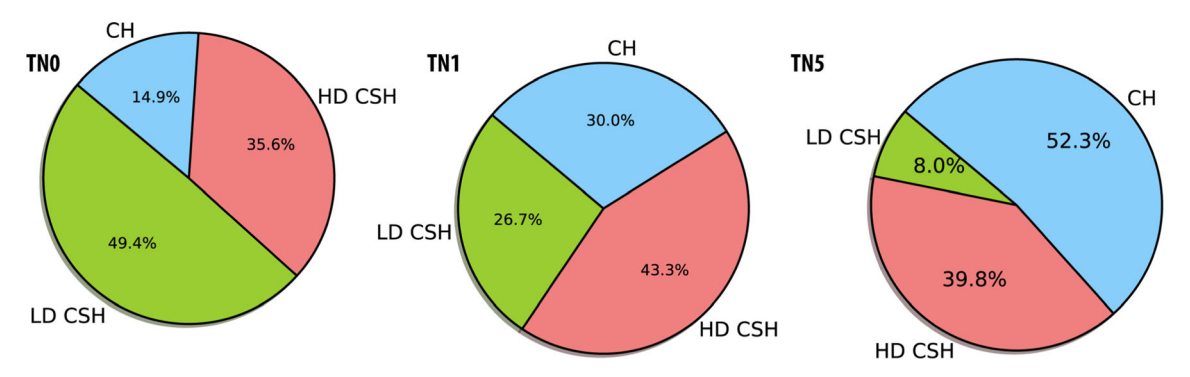


Figure 9 Percentage of calcium silicate hydrate phases for Portland cement TiO₂ nanocomposites. LD CSH = low-density C–S–H. HD CSH = high-density C–S–H. CH = calcium hydroxide.



Discussion

Nano-TiO₂ accelerates high-density C-S-H formation

The FTIR results and the statistical deconvolution analysis show that nano-TiO₂ promotes the growth of high-density C–S–H and calcium hydroxide. Other researchers had reported increased crystallization of calcium hydroxide based on X-ray diffraction observations [15, 22]. Furthermore, we observe an increase in high-density C–S–H, which is a novel insight. High-density C–S–H exhibits small gel pores in the order of a few nanometers [36]. Thus, an increase in high-density C–S–H will result in a reduction in the fraction of mesopores, thereby explaining the refinement in pore structure reported in prior studies [12, 18, 19].

High-stiffness C-S-H holds the key to improvements in the mechanical and transport properties

In turn, the high polymerization of high-density C–S–H and calcium hydroxide leads to a tremendous increase in mechanical properties. As shown in Fig. 2, the stiffness-to-weight ratio is multiplied by 1.74, and the strength-to-weight ratio is enhanced by 1.33 through simply adding 5 wt% nano-TiO₂. This significant gain in stiffness can be explained by the close-packed atomic structure of high-density C–S–H at the nanometer length scale, and the redistribution of the porosity into small gel pores 1.2–2 nm in size.

The close-packed structure of high-density C–S–H is also at the origin of the reported strengthening of nano-TiO₂-modified cement [11–15]. Prior investigation [39] has shown that particle-to-particle contact forces drive the macroscopic cement strength properties at the nanoscale. An essential consequence of the close-packed density of high-density C–S–H is the high atomic coordination number. As a result, the composite can absorb mechanical energy and readily dissipate that energy at the nanometer length scale in the form of heat via grain-to-grain friction.

Furthermore, we can tie the increased growth of high-density C–S–H to enhanced drying shrinkage behavior and creep response using the colloidal [36, 40] and nanogranular [41] models for C–S–H. Within the colloidal model for C–S–H, irreversible shrinkage occurs due to irreversible volume changes

following the packing of globules under the drying stress. These irreversible volume changes tend to be more pronounced in low-density C–S–H as low-density C–S–H contains 5–12 nm large gel pores at a scale of 60–100 nm. In contrast, high-density C–S–H and calcium hydroxide tend to be more dimensionally stable and therefore act as geometrical constraints. Thus, an increase in the volume fraction of high-density C–S–H will lead to reduced drying shrinkage as observed for nano-TiO₂-modified cement [19].

Within the nanogranular model for C-S-H, the creep response results from thermally activated globule movements. In turn, the creep obeys a logarithmic law and the logarithmic creep modulus depends on the distribution of low-density C-S-H, high-density C-S-H, and high-density C-S-H [41]. Due to its low packing density, low-density C-S-H exhibits a low value of the logarithmic creep modulus. Meanwhile, the logarithmic creep modulus values for high-density C-S-H and calcium hydroxide (or ultra-high-density C–S–H) are almost the double of that of low-density C-S-H [29]. Thus, a higher fraction of high-density C-S-H, promoted by the catalytic effect of nano-TiO2, will generate considerable increases in the creep resistance and hence the long-term mechanical integrity of nano-TiO2-modified cement.

The higher dimensional stability of high-density C–S–H can explain the reported decrease in water permeability and water absorption for nano-TiO₂-modified cement [18]. This reported decrease is also due to the virtual absence of large gel pores—5–12 nm big—which abound in low-density C–S–H. Thus, our discovery of an increase in high-density C–S–H following modification with nano-TiO₂ is fundamental to understanding the significant improvement in mechanical properties, durability, and transport properties.

Conclusions

We investigated the impact of nano-TiO₂ on the nanostructure and mechanical properties of Portland cement paste. We synthesized nano-modified Portland cement paste with 1 wt% and 5 wt% nano-TiO₂. We performed statistical nanoindentation and microscopic scratch tests integrated with environmental scanning electron microscopy and Fourier



transform infrared spectroscopy studies. We employed Jennings' colloidal model and Ulm's nanogranular model of cement paste to understand the behavior. These are our main findings:

- Nano-TiO₂ promotes calcium hydroxide growth, leading to a 101% and a 251% increase, respectively.
- Nano-TiO₂ promotes the growth of high-density C-S-H, leading to increases of 22% and 12%, respectively.
- Nano-TiO₂ leads to an improvement in stiffness, 16% and 83%, hardness, 37% and 40%, and an improvement of the stiffness-to-weight and of the strength-to-weight ratios.
- Nano-TiO₂ leads to an increase in fracture toughness, 3% and 11%, and a 30% reduction in crack width.
- The increase in stiffness following cement modification with nano-TiO₂ is due to the closely packed nano-structure of high-density C-S-H.
- The increase in strength following nano-TiO₂ modification is due to the high atomic coordination number of high-density C-S-H.
- The decrease in the drying shrinkage and the decrease in the creep deformation are due to the high dimensional stability of high-density C-S-H.

Acknowledgements

This work was supported by the National Science Foundation under Grant No. CMMI 1829101. This work made use of the EPIC facility of Northwestern University's NUANCE Center, which has received support from the Soft and Hybrid Nanotechnology Experimental (SHyNE) Resource (NSF ECCS-1542205); the MRSEC program (NSF DMR-1720139) at the Materials Research Center; the International Institute for Nanotechnology (IIN); the Keck Foundation; and the State of Illinois, through the IIN. A special thanks to Jiaxin Chen for conducting the FTIR tests.

Funding

This study was funded by the National Science Foundation under Grant No. CMMI 1829101.

Compliance with ethical standards

Conflict of interest The author declares that she has no conflict of interest.

Electronic supplementary material: The online version of this article (https://doi.org/10.1007/s108 53-020-04847-5) contains supplementary material, which is available to authorized users.

References

- Nazari A, Riahi S, Riahi S, Shamekhi SF, Khademno A
 (2010) Mechanical properties of cement mortar with Al₂O₃
 nanoparticles. J Am Sci 6(4):94–97
- [2] Gaitero JJ, Campillo I, Guerrero A (2008) Reduction of the calcium leaching rate of cement paste by addition of silica nanoparticles. Cem Conc Res 38(8-9):1112–1118. https://d oi.org/10.1016/j.cemconres.2008.03.021
- [3] Stefanidou M, Papayianni I (2012) Influence of nano-SiO₂ on the Portland cement pastes. Comp Part B Eng 43(6):2706–2710. https://doi.org/10.1016/j.compositesb.201 1.12.015
- [4] Liu J, Li Q, Xu S (2015) Influence of nanoparticles on fluidity and mechanical properties of cement mortar. Constr Build Mater 101:892–901. https://doi.org/10.1016/j.conbuildmat.2015.10.149
- [5] Tobon JI, Paya J, Restrepo OJ (2015) Study of durability of Portland cement mortars blended with silica nanoparticles. Constr Build Mater 80:92–97. https://doi.org/10.1016/j.conb uildmat.2014.12.074
- [6] Kawashima S, Hou P, Corr DJ, Shah SP (2013) Modification of cement-based materials with nanoparticles. Cem Concr Comp 36:8–15. https://doi.org/10.1016/j.cemconcomp.2012. 06.012
- [7] Shaikh FUA, Supit SWM, Sarker PK (2014) A study on the effect of nano silica on compressive strength of high volume fly ash mortars and concretes. Mater Des 60:433–442. http s://doi.org/10.1016/j.matdes.2014.04.025
- [8] Cardenas C, Tobon JI, Garcia C, Vila J (2012) Functionalized building materials: photocatalytic abatement of NO_x by cement pastes blended with TiO₂ nanoparticles. Constr Build Mater 36:820–825. https://doi.org/10.1016/j.conbuildmat.20 12.06.017
- [9] Diamanti MV, Del Curto B, Ormellese M, Pedeferri MP (2013) Photocatalytic and self-cleaning activity of colored mortars containing TiO₂. Constr Build Mater 46:167–174. h ttps://doi.org/10.1016/j.conbuildmat.2013.04.038



- [10] Perez-Nicolas M, Balbuena J, Cruz-Yusta M, Sanchez L, Navarro-Blasco I, Fernandez JM, Alvarez JI (2015) Photocatalytic NO_x abatement by calcium aluminate cements modified with TiO₂: improved NO₂ conversion. Cem Concr Res 70:67–76. https://doi.org/10.1016/j.cemconres.2015.01. 011
- [11] Nazari A, Riahi S, Riahi S, Shamekhi SF, Khademno A (2010) Assessment of the effects of the cement paste composite in presence TiO₂ nanoparticles. Am Sci 6(4):43–46
- [12] Chen J, Kou SC, Poon CS (2012) Hydration and properties of nano-TiO₂ blended cement composites. Cem Concr Comp 34(5):642–649. https://doi.org/10.1016/j.cemconcomp.2012. 02.009
- [13] Nazari A, Riahi S (2011) The effects of TiO₂ nanoparticles on physical, thermal and mechanical properties of concrete using ground granulated blast furnace slag as binder. Mater Sci Eng A 528(4-5):2085–2092. https://doi.org/10.1016/j.m sea.2010.11.070
- [14] Feng D, Xie N, Gong C, Leng Z, Xiao H, Li H, Shi X (2013)

 Portland cement paste modified by TiO₂ nanoparticles: a microstructure perspective. Industr Eng Chem Res 52(33):11575–11582. https://doi.org/10.1021/ie4011595
- [15] Jalal M, Fathi M, Farzad M (2013) Effects of fly ash and TiO₂ nanoparticles on rheological, mechanical, microstructural and thermal properties of high strength self compacting concrete. Mech Mater 61:11–27. https://doi.org/10.1016/j.m echmat.2013.01.010
- [16] Wang L, Zhang H, Gao Y (2018) Effect of TiO₂ nanoparticles on physical and mechanical properties of cement at low temperatures. Adv Mater Sci Eng. https://doi.org/10.11 55/2018/8934689
- [17] Senff L, Hotza D, Lucas S, Ferreira VM, Labrincha JA (2012) Effect of nano-SiO₂ and nano-TiO₂ addition on the rheological behavior and the hardened properties of cement mortars. Mater Sci Eng A 532:354–361. https://doi.org/10. 1016/j.msea.2011.10.102
- [18] Ma B, Li H, Mei J, Li X, Chen F (2015) Effects of nano-TiO₂ on the toughness and durability of cement-based material. Adv Mater Sci Eng. https://doi.org/10.1155/2015/ 583106
- [19] Zhang R, Cheng X, Hou P, Ye Z (2015) Influences of nano-TiO₂ on the properties of cement-based materials: hydration and drying shrinkage. Constr Build Mater 81:35–41. http s://doi.org/10.1016/j.conbuildmat.2015.02.003
- [20] Lee BY, Kurtis KE (2012) Proposed acceleratory effect of TiO2 nanoparticles on belite hydration: preliminary results. J Am Ceram Soc 95(1):365–368. https://doi.org/10.1111/j. 1551-2916.2011.04937.x
- [21] Jayapalan AR, Lee BY, Fredrich SM, Kurtis KE (2010) Influence of additions of anatase TiO₂ nanoparticles on

- early-age properties of cement-based materials. Transp Res Rec 2141(1):41–46. https://doi.org/10.3141/2141-08
- [22] Nazari A, Riahi S (2010) The effect of TiO₂ nanoparticles on water permeability and thermal and mechanical properties of high strength self-compacting concrete. Mater Sci Eng A 528(2):756–763. https://doi.org/10.1016/j.msea.2010.09.074
- [23] Meng T, Yu Y, Qian X, Zhan S, Qian K (2012) Effect of nano-TiO₂ on the mechanical properties of cement mortar. Constr Build Mater 29:241–245. https://doi.org/10.1016/j.conbuildmat.2011.10.047
- [24] Akono AT, Ulm FJ (2014) An improved technique for characterizing the fracture toughness via scratch test experiments. Wear 313:117–124. https://doi.org/10.1016/j.wear.2 014.02.015
- [25] Akono AT, Randall NX, Ulm FJ (2012) Experimental determination of the fracture toughness via micro scratch tests: application to polymers, ceramics and metals. J Mat Res 27:485–493. https://doi.org/10.1557/jmr.2011.402
- [26] Oliver WC, Pharr GM (2004) Measurement of hardness and elastic modulus by instrumented indentation: advances in understanding and refinements to methodology. J Mat Res 19(1):3–20. https://doi.org/10.1557/jmr.2004.19.1.3
- [27] Oliver WC, Pharr GM (1992) An improved technique for determining hardness and elastic modulus using load and displacement sensing indentation experiments. J Mat Res 7(6):1564–1583. https://doi.org/10.1557/JMR.1992.1564
- [28] Vandamme M (2008) The nanogranular origin of concrete creep: a nanoindentation investigation of microstructure and fundamental properties of calcium-silicate-hydrates. PhD dissertation, Massachusetts Institute of Technology.
- [29] Vandamme M, Ulm FJ (2013) Nanoindentation investigation of creep properties of calcium silicate hydrates. Cem Concr Res 52:38–52. https://doi.org/10.1016/j.cemconres.2013.05. 006
- [30] Sorelli L, Constantinides G, Ulm FJ, Toutlemonde F (2008) The nano-mechanical signature of ultra high performance concrete by statistical nanoindentation techniques. Cem Concr Res 38(12):1447–1456. https://doi.org/10.1016/j.cem conres.2008.09.002
- [31] Cotterell B, Mai YW (1987) Crack growth resistance curve and size effect in the fracture of cement paste. J Mat Sci 22(8):2734–2738
- [32] Hu X, Wittmann F (2000) Size effect on toughness induced by crack close to free surface. Eng Fract Mech 65(2-3):209–221. https://doi.org/10.1016/S0013-7944(99)00123-X
- [33] Pellenq RJM, Van Damme H (2004) Why does concrete set?: The nature of cohesion forces in hardened cementbased materials. MRS Bull 29(5):319–323. https://doi.org/ 10.1557/mrs2004.97



- [34] Shahsavari R, Buehler MJ, Pellenq RJM, Ulm FJ (2009) First-principles study of elastic constants and interlayer interactions of complex hydrated oxides: case study of tobermorite and jennite. J Am Cer Soc 92(10):2323–2330. h ttps://doi.org/10.1111/j.1551-2916.2009.03199.x
- [35] Jennings HM (2000) A model for the microstructure of calcium silicate hydrate in cement paste. Cem Concr Res 30(1):101–116. https://doi.org/10.1016/S0008-8846(99)002 09-4
- [36] Jennings HM (2004) Colloid model of C- S- H and implications to the problem of creep and shrinkage. Mater Struct 37(1):59-70
- [37] Jennings HM (2008) Refinements to colloid model of CSH in cement: CM-II. Cem Concr Res 38(3):275–289. https://d oi.org/10.1016/j.cemconres.2007.10.006
- [38] Tennis PD, Jennings H (2000) A model for two types of calcium silicate hydrate in the microstructure of Portland

- cement pastes. Cem Concr Res 30(6):855–863. https://doi.org/10.1016/S0008-8846(00)00257-X
- [39] Constantinides G, Ulm FJ (2007) The nanogranular nature of C-S-H. J Mech Phys Sol 55(1):64-90. https://doi.org/10. 1016/j.jmps.2006.06.003
- [40] Thomas JJ, Jennings HM (2006) A colloidal interpretation of chemical aging of the CSH gel and its effects on the properties of cement paste. Cem Concr Res 36(1):30–38. https://d oi.org/10.1016/j.cemconres.2004.10.022
- [41] Vandamme M, Ulm FJ (2009) Nanogranular origin of concrete creep. Proc Natl Acad Sci 106(26):10552–10557. h ttps://doi.org/10.1073/pnas.0901033106

Publisher's Note Springer Nature remains neutral with regard to jurisdictional claims in published maps and institutional affiliations.

